Science Advances

▲AAAS

Supplementary Materials for

Angle-multiplexed all-dielectric metasurfaces for broadband molecular fingerprint retrieval

Aleksandrs Leitis, Andreas Tittl, Mingkai Liu, Bang Hyun Lee, Man Bock Gu, Yuri S. Kivshar, Hatice Altug*

*Corresponding author. Email: hatice.altug@epfl.ch

This PDF file includes:

Supplementary Materials

Supplementary Text

The effective impedance model of the quasi-BICs

In order to obtain a deeper understanding of the resonance shift of the quasi-BICs supported by the zig-zag dipole array, we developed a semi-analytical model based on the effective impedance of the array (27). Assuming the collective mode of the array is built on the electric dipole mode of the meta-atom, the interaction of the zig-zag array and incident wave can be expressed as

$$\vec{Z}\mathbf{I} = \mathbf{V} \tag{1}$$

where

$$\vec{Z} = \begin{bmatrix} Z_{self} & Z_{mut} \\ Z_{mut} & Z_{self} \end{bmatrix} \tag{2}$$

is the effective impedance of the collective mode; $\mathbf{I} = [I_1, I_2]^T$ is the corresponding current amplitude of the dipoles, and $\mathbf{V} = [V_1, V_2]^T$ is the effective electromotive force, with subscripts "1" and "2" denoting the two different orientation angles of the dipoles.

We are interested in the angle-dependent resonance shift, which can be understood by analyzing the behaviour of the impedance. The expressions

$$Z_{self} = \sum_{m=-\infty}^{\infty} \sum_{n=-\infty}^{\infty} Z_S^{(m,n)} e^{i(m\beta_x P_x + n\beta_y P_y)} \tag{3}$$

and

$$Z_{mut} = \sum_{m=-\infty}^{\infty} \sum_{n=-\infty}^{\infty} Z_M^{(m,n)} e^{i\beta_x P_x/2} e^{i(m\beta_x P_x + n\beta_y P_y)} \tag{4}$$

describe the lattice sum of the complex electromagnetic interaction of the meta-atoms, where the subscript "self" ("mut") denotes that the lattice sum is performed over meta-atoms with the same (different) orientation angles, and $Z_S^{(m,n)}$ and $Z_M^{(m,n)}$ are the impedance elements that describe the interaction between the meta-atoms located at the lattice sites (0,0) and (m,n). β_x and β_y are the transverse wave-vectors of the collective mode along the x and y directions, respectively.

Typically, a system described by Eq. (1) can support two normal modes: a symmetric mode ($I_1 = I_2$) and an antisymmetric mode ($I_1 = -I_2$). The qusi-BICs correspond to the antisymmetric mode, and the effective impedance of this mode can be described by

$$Z_{eff} = Z_{self} - Z_{mut} = \sum_{m,n} (Z_S^{(m,n)} - e^{i\beta_x P_x /2} Z_M^{(m,n)}) e^{i(m\beta_x P_x + n\beta_y P_y)} \tag{5}$$

For loss-less meta-atoms positioned in a homogenous environment, the impedance elements $Z_S^{(m,n)}$ and $Z_M^{(m,n)}$ can be calculated deterministically from the normalized current $\mathbf{j}(\mathbf{r})$ and charge $q(\mathbf{r})$ distributions of the meta-atoms (32)

$$Z_S^{(m,n)} = \frac{i}{4\pi} \int_{V_1} \int_{V_1} \left(-\omega\mu \mathbf{j}_1^{(0,0)} \cdot \mathbf{j}_1^{(m,n)} + \frac{q_1^{(0,0)} q_1^{(m,n)}}{\omega\varepsilon} \right) \frac{e^{ik|\mathbf{r}_1^{(0,0)} - \mathbf{r}_1^{(m,n)}|}}{|\mathbf{r}_1^{(0,0)} - \mathbf{r}_1^{(m,n)}|} d^3\mathbf{r}_1^{(0,0)} d^3\mathbf{r}_1^{(m,n)} \tag{6}$$

$$Z_M^{(m,n)} = \frac{i}{4\pi} \int_{V_1} \int_{V_2} \left(-\omega\mu \mathbf{j}_1^{(0,0)} \cdot \mathbf{j}_2^{(m,n)} + \frac{q_1^{(0,0)} q_2^{(m,n)}}{\omega\varepsilon} \right) \frac{e^{ik|\mathbf{r}_1^{(0,0)} - \mathbf{r}_2^{(m,n)}|}}{|\mathbf{r}_1^{(0,0)} - \mathbf{r}_2^{(m,n)}|} d^3\mathbf{r}_1^{(0,0)} d^3\mathbf{r}_2^{(m,n)} \tag{7}$$

The subscripts "1" and "2" denote the two orientation angles of the meta-atoms, and the superscript (m,n) denotes the lattice site.

The terms for interacting currents $\mathbf{j}^{(0,0)} \cdot \mathbf{j}^{(m,n)}$ correspond to the complex magnetic interaction power, while the terms for interacting charges $q^{(0,0)} q^{(m,n)}$ correspond to the complex electric interaction power (32), which can be further denoted as the inductance, capacitance and resistance

$$L_S^{(m,n)} = \mathrm{Re}\left[\frac{1}{4\pi} \int\int_{V_1 V_1} \mu \mathbf{j}_1^{(0,0)} \cdot \mathbf{j}_1^{(m,n)} \frac{e^{ik|\mathbf{r}_1^{(0,0)}-\mathbf{r}_1^{(m,n)}|}}{|\mathbf{r}_1^{(0,0)}-\mathbf{r}_1^{(m,n)}|} d^3\mathbf{r}_1^{(0,0)} d^3\mathbf{r}_1^{(m,n)} \right] \tag{8}$$

$$L_M^{(m,n)} = \mathrm{Re}\left[\frac{1}{4\pi} \int\int_{V_1 V_2} \mu \mathbf{j}_1^{(0,0)} \cdot \mathbf{j}_2^{(m,n)} \frac{e^{ik|\mathbf{r}_1^{(0,0)}-\mathbf{r}_2^{(m,n)}|}}{|\mathbf{r}_1^{(0,0)}-\mathbf{r}_2^{(m,n)}|} d^3\mathbf{r}_1^{(0,0)} d^3\mathbf{r}_2^{(m,n)} \right] \tag{9}$$

$$1/C_S^{(m,n)} = \mathrm{Re}\left[\frac{1}{4\pi\varepsilon} \int\int_{V_1 V_1} q_1^{(0,0)} q_1^{(m,n)} \frac{e^{ik|\mathbf{r}_1^{(0,0)}-\mathbf{r}_1^{(m,n)}|}}{|\mathbf{r}_1^{(0,0)}-\mathbf{r}_1^{(m,n)}|} d^3\mathbf{r}_1^{(0,0)} d^3\mathbf{r}_1^{(m,n)} \right] \tag{10}$$

$$1/C_M^{(m,n)} = \mathrm{Re}\left[\frac{1}{4\pi\varepsilon} \int\int_{V_1 V_2} q_1^{(0,0)} q_2^{(m,n)} \frac{e^{ik|\mathbf{r}_1^{(0,0)}-\mathbf{r}_2^{(m,n)}|}}{|\mathbf{r}_1^{(0,0)}-\mathbf{r}_2^{(m,n)}|} d^3\mathbf{r}_1^{(0,0)} d^3\mathbf{r}_2^{(m,n)} \right] \tag{11}$$

$$R_S^{(m,n)} = \mathrm{Re}\left[Z_S^{(m,n)} \right] \tag{12}$$

$$R_M^{(m,n)} = \mathrm{Re}\left[Z_M^{(m,n)} \right] \tag{13}$$

Therefore, the effective impedance of the quasi-BIC can be re-expressed as

$$Z_{eff} = -i\omega L_{eff} + i/(\omega C_{eff}) + R_{eff} \tag{14}$$

where

$$L_{eff} = \sum_{m,n} (L_S^{(m,n)} - e^{i\beta_x P_x/2} L_M^{(m,n)}) e^{i(m\beta_x P_x + n\beta_y P_y)} \tag{15}$$

$$1/C_{eff} = \sum_{m,n}(1/C_S{}^{(m,n)} - e^{i\beta_x P_x/2}1/C_M{}^{(m,n)})e^{i(m\beta_x P_x + n\beta_y P_y)} \qquad (16)$$

$$R_{eff} = \sum_{m,n}(R_S{}^{(m,n)} - e^{i\beta_x P_x/2}R_M{}^{(m,n)})e^{i(m\beta_x P_x + n\beta_y P_y)} \qquad (17)$$

are the effective inductance, elastance (inverse of capacitance), and resistance due to radiative loss, respectively.

For the plot shown in Fig. 2F of the main text, we calculate an array of line dipoles embedded in a homogeneous environment with a refractive index of one. The current distribution **j** of the line dipoles is approximated by a sinusoidal function. The zeros of the reactance, i.e. $\text{Im}(Z_{eff}) = -\omega L_{eff} + 1/(\omega C_{eff}) = 0$, mark the resonant frequencies. We find that the angle-dependant resonant shift shown in Fig. 2C can be reproduced very well even with a simplified line-dipole model.

Due to the anisotropy of the interaction among the in-plane dipoles, the spatial distribution of the impedance elements $Z_S{}^{(m,n)}$ and $Z_M{}^{(m,n)}$ are also anisotropic, as shown in fig. S1. As a result, when retardation is increased along the x or y-direction, the lattice sum changes in different ways. Further analysis shows that for the TM_x mode, the effective elastance $1/C_{eff}$ decreases while the effective inductance L_{eff} increases with the incident angle, leading to a decreased effective reactance and a red-shift of the resonance. In contrast, a reverse trend is observed for TE_y mode, which results in a resonance blue-shift, as shown in fig. S2.

Resonance properties

The extracted resonance frequencies for all angle steps are displayed in fig. S3A, showing continuous resonance frequency tunability in the range of 1100 to 1800 cm^{-1} with average resonance step size of 1.4 cm^{-1} corresponding to a 0.2 degree angular step. The resonance position for different light incidence angles agrees very well with the simulation data (Fig. 2C). The resonance peak reflectance for different light incidence angles is displayed in fig. S3B. The non-uniform peak reflectance for the TM_x mode arises from a 1.7 degree angular spread of the incident light, which produces significant peak attenuation due to averaging of the individual resonance line shapes. In general, resonances with higher Q-factor are more susceptible to this inhomogeneous broadening effect, explaining the link between the increasing Q-factor and the decreasing reflectance amplitude for higher incidence angles. In contrast, the pronounced drop in peak reflectance for the TE_y mode at higher light incidence angles can be explained by the coupling to the first grating order. For completeness, the extracted full width at half maximum of the resonance at different light incidence angles is displayed in fig. S3C. The resonance quality factor for both TE_y and TM_x modes are shown in the fig. S3D, with

an average quality factor of 121. The quality factor for the TM mode increases upon higher light incidence angles due to increased effective inductance (fig. S2). The resonance Q factor can be calculated by $Q = \omega_0 L/R$, where ω_0 is the resonance frequency, L is the effective inductance and R is the effective resistance. To compensate for the increased absorbance signal associated with the increased quality factor, the spectrograms have been normalized by the Q factor.

Effective spectral resolution for total reflectance operation

In the total reflectance operation scheme, which utilizes the spectrally integrated signal from the metasurface, the effective spectral resolution is influenced by both the resonance step size and the Q-factor of the resonances. We implemented a temporal coupled mode theory (TCMT) approach to model the influence of two narrow vibrational bands on the line shape of a high-Q resonance, based on previous calculations reported in Ref. (33). Specifically, the high-Q nanophotonic resonators were described using their resonance frequency ω_R and damping rate γ_R. The two narrow vibrational bands were modeled using identical damping rates $\gamma_V^{(1)} = \gamma_V^{(2)} = \gamma_V = 0.1 \text{ cm}^{-1}$ and were assumed to be spaced equally around a center frequency of $\omega_c = 1600 \text{ cm}^{-1}$ with spectral separation $\Delta\omega$, which yields the individual spectral positions of the bands as $\omega_V^{(1,2)} = \omega_c \pm \Delta\omega/2$. The coupling constants between the two non-radiative vibrational modes and the radiative resonator mode are fixed as $\mu^{(1)} = \mu^{(2)} = \mu = 0.05 \text{ cm}^{-1}$.

The reflection amplitude of the resonator coupled to the two vibrational bands is then given as (see Ref. (33) for details)

$$r = \gamma_R / \left[i\left(\omega - \omega_A - \omega_\mu \right) + \gamma_R + \gamma_\mu \right] \tag{18}$$

where

$$\omega_\mu = \Sigma_{i=1}^2 \frac{\mu^2 \left(\omega - \omega_V^{(i)} \right)}{\left(\omega - \omega_V^{(i)} \right)^2 + \gamma_V^2} \tag{19}$$

and

$$\gamma_\mu = \Sigma_{i=1}^2 \frac{\mu^2 \gamma_V}{\left(\omega - \omega_V^{(i)} \right)^2 + \gamma_V^2} \tag{20}$$

To assess the spectral resolution, we calculated reflectance spectra for different values of the resonance Q-factor and spectral separation of the bands over a wide parameter range. For every point in this parameter space, we then evaluated whether the two narrow bands could still be identified from the integrated reflectance signals. The resulting plot of the spectral resolution (i.e., the lowest spectral band separation that can still be identified for a given Q-factor) is shown in fig. S4. The numerical modeling shows that the maximum achievable resolution of our metasurface-based approach is around 4 cm^{-1} using a resonance step size of 0.5 cm^{-1}. Since our experiments target vibrational bands with spectral feature sizes much larger than this value (see, e.g., Fig. 4C in the main text of the manuscript), we chose a resonance step size of 1.5 cm^{-1}, which results in an effective spectral resolution of around 5 cm^{-1}. Importantly, highly competitive spectral resolutions below 2 cm^{-1} can be achieved by using a metasurface with increased, but still experimentally feasible quality factors (18).

AFR signal and Fresnel reflection compensation.

The total reflectance signal is directly dependent on the resonance background, the higher the background reflection the lower the total reflectance signal modulation before and after analyte adsorption. Therefore it is essential to minimize the background reflection for broadband operation. Assuming TE$_y$ mode, the resonance reflectance background will increase upon increasing light incidence angles, thus the signal modulation will be lower for higher light incidence angles. To compensate for the signal drop, we calculated the resonance background at each light incidence angle (fig. S5A). To show that this background subtraction compensates for the Fresnel reflection even after analyte deposition, we show a reflectance spectrum of streptavidin with subtracted background reflectance from the reference measurement (fig. S5B).

The AFR signal of streptavidin for all light incidence angles and without any background subtraction is displayed in fig. S5C. The corresponding integration range is from 1050 cm^{-1} to 1830 cm^{-1}. The AFR curve clearly retrieves the characteristic amide I and amide II vibrational bands, however, due to the increased reflection background at larger light incidence angles, the amide I band appears as having lower absorption strength compared to the amide II band.

To correct the signal attenuation and retrieve precise relative absorption strength of the analyte, we calculate the total reflectance from the background reflection and subtract it from both the reference and analyte total reflectance signal

$$\text{AFR}_C = -\log(I_A - I_B / I_R - I_B) \tag{21}$$

where, I_A is the total reflectance signal of the metasurface coated with analyte, I_B is the total reflectance signal of the background and I_R is the total reflectance signal of the

clean metasurface measurement. The use of background correction clearly compensates for the signal decrease at higher light incidence angles which corrects also the relative absorption strength (fig. S5D).

Measurement noise evaluation and limit of detection

The experimental noise was evaluated by two consecutive measurements of an empty chip for all 236 light incidence angles, where the first measurement was taken as a reference measurement and the second as a noise measurement. The noise of the absorbance was calculated from the total reflectance signal with integration range from 1050 cm^{-1} to 1830 cm^{-1} via

$$AFR_N = -\log(I_N/I_R) \tag{22}$$

where AFR_N is noise signal, I_N is the total reflectance signal of noise measurement and I_R is the total reflectance signal from the reference measurement. The absorbance noise values were calculated for all 236 angle steps and are displayed in the fig. S6A. The total noise level was quantified by calculating the standard deviation of the noise signal, which results in an experimental noise level value of

$$AFR_{\text{Nrms}} = \sqrt{\frac{1}{p}\sum_{k=1}^{p}\left(AFR_{Ni}^{(k)}\right)^2} = 1.57 \tag{23}$$

where $AFR_N^{(k)}$ denotes the noise value at a specific angular position with $k = 1, \cdots, p$, and $p = 236$, consistent with the angular steps.

The sensors can reliably detect signals that are three times above the noise level. To evaluate the limit of detection of our AFR method, we measured the AFR signal from physisorbed streptavidin monolayer, see fig. S6B. The peak signal value is $AFR_{Strep} = 86.5 \, (a.u.)$ whereas the noise $3\sigma = 4.7 \, (a.u.)$, this shows that we could detect 18.4 times less molecules per unit area. To calculate the minimum amount of molecules that we could detect with the AFR method, we need to calculate how many streptavidin molecules are needed to uniformly cover 1 µm^2 area. The molecular weight of the streptavidin molecule is 55 kDa, which would correspond to 4.8 nm diameter considering the most dense packing of the atoms (34). This results in 55200 molecules per 1 µm^2, assuming a monolayer coverage of the streptavidin molecules. Knowing, that the absorption signal from a monolayer of streptavidin is 18.4 times above the 3σ noise floor, the limit of detection is 3000 molecules per µm^2 area which would correspond to 0.27 pg/mm^2 surface mass sensitivity.
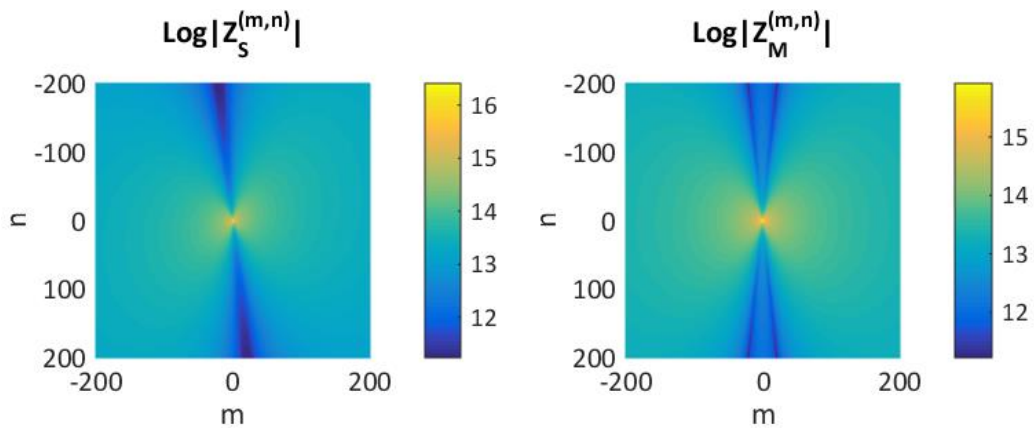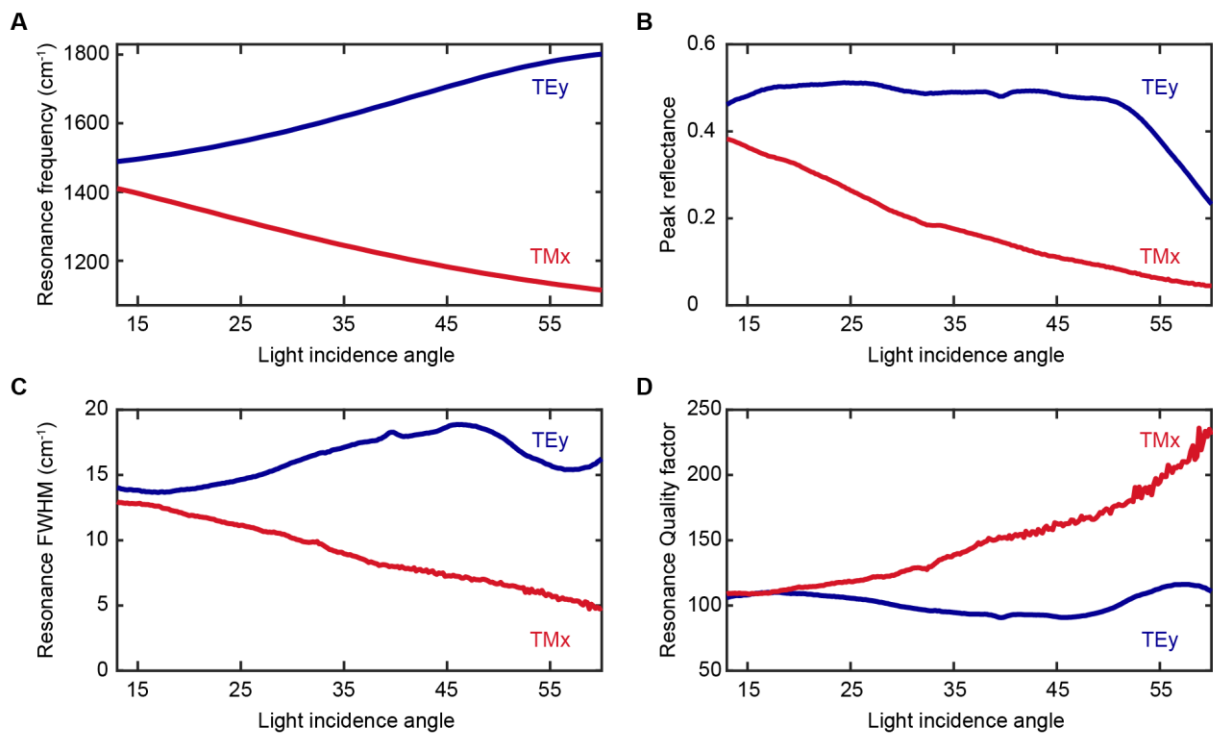
**Fig. S1.** The lattice distribution of the impedance element $Z_S^{(m,n)}$ **and** $Z_M^{(m,n)}$.
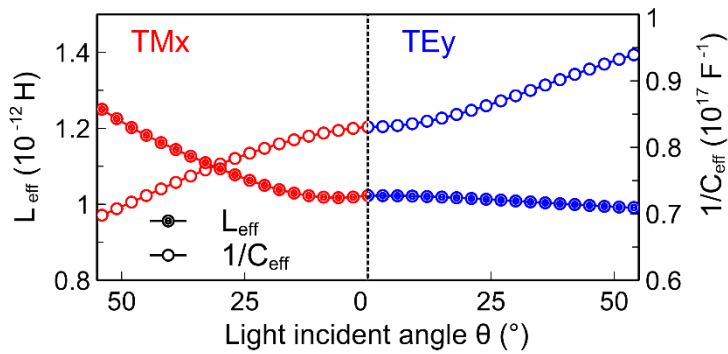
Fig. S2. The change of the effective inductance and elastance under different incident angles. To avoid the complexity introduced by the 1st order diffraction, the effective inductance and elastance are evaluated at 1100 cm^{-1}.

**Fig. S3. Experimental data of resonance position and quality factor.** (**A**) Experimental data of the resonance position for the TE_y and TM_x modes. (**B**) Resonance peak reflectance for TE_y and TM_x modes. (**C**) Resonance full width half maximum for TE_y and TM_x modes. (**D**) Resonance quality factor for TE_y and TM_x modes.
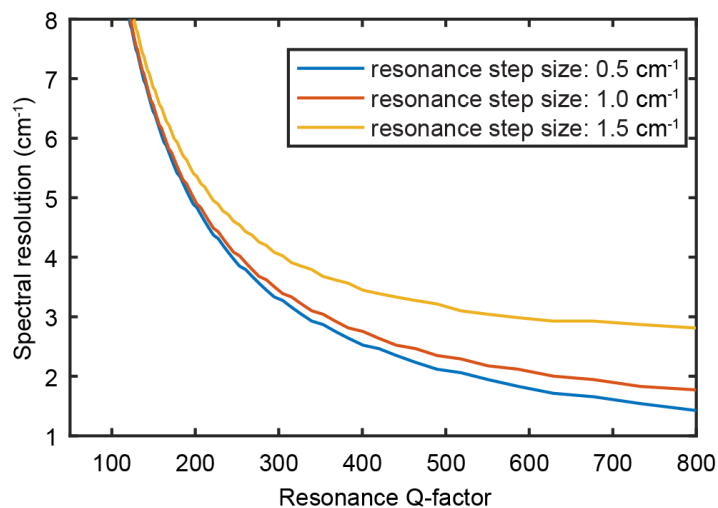
Fig. S4. Spectral resolution as a function of Q-factor for different values of the resonance step size.
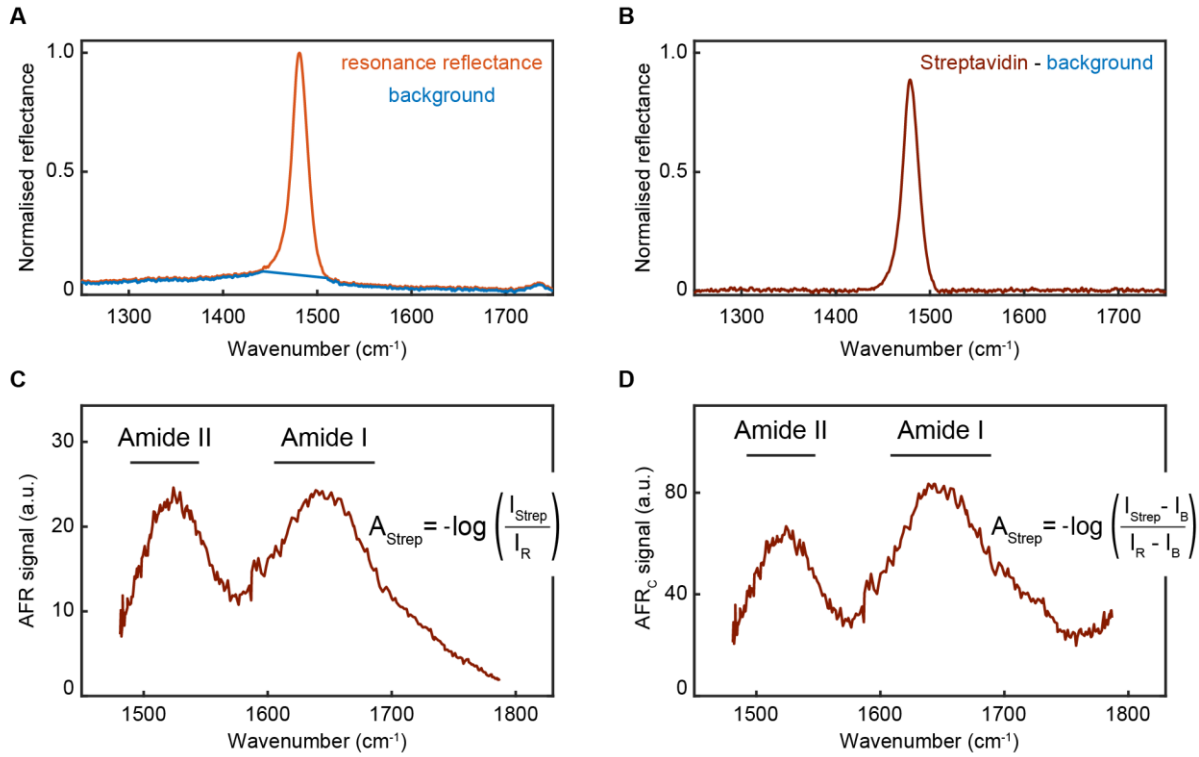
Fig. S5. Resonance background calculation and AFR signal correction. (**A**) Normalised reflectance of the metasurface at 13 degree light incidence angle and the calculated resonance background. (**B**) Metasurface reflectance at 13 degree light incidence angle after streptavidin adsorption with subtracted resonance background. (**C**) AFR signal with integration range from 1050 cm^{-1} to 1830 cm^{-1}. (**D**) AFR signal with the subtraction of background reflection.
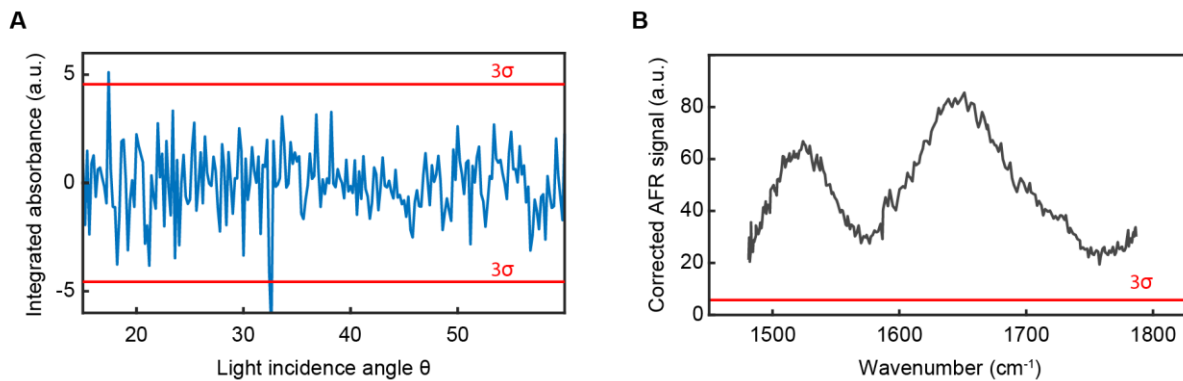
Fig. S6. Noise and limit of detection. (**A**) measured AFR signal noise from two consecutive measurements of all angle steps (**B**) The AFR 3σ comparison with the AFR signal from monolayer of streptavidin.